

Effect of Coupled Flow and Geomechanics on Transport of a Fluid Slug in a Stress-sensitive Reservoir

Tran, M.

University of Southern California, Los Angeles, California, United States of America

Aminzadeh, F. and Jha, B.

University of Southern California, Los Angeles, California, United States of America

Copyright 2018 ARMA, American Rock Mechanics Association

This paper was prepared for presentation at the 52nd US Rock Mechanics / Geomechanics Symposium held in Seattle, Washington, USA, 17–20 June 2018. This paper was selected for presentation at the symposium by an ARMA Technical Program Committee based on a technical and critical review of the paper by a minimum of two technical reviewers. The material, as presented, does not necessarily reflect any position of ARMA, its officers, or members. Electronic reproduction, distribution, or storage of any part of this paper for commercial purposes without the written consent of ARMA is prohibited. Permission to reproduce in print is restricted to an abstract of not more than 200 words; illustrations may not be copied. The abstract must contain conspicuous acknowledgment of where and by whom the paper was presented.

ABSTRACT: We develop a 2D fully-coupled flow and geomechanical simulator to model the movement, mixing and spreading of a slug through a deformable reservoir. The mechanics problem is discretized using the finite element method, and the flow problem is discretized using the finite volume method. A simultaneous solver is used at each time step to concurrently solve the coupled problem for pressure and displacement fields. The velocity field constructed from the solution is input to the transport solver, which solves the convection-diffusion equation for the slug concentration field. A sensitivity analysis is performed to evaluate the dependence of global transport characteristics such as the slug breakthrough time, drainage time and the degree of mixing on the geomechanical coupling. Results are obtained for different levels of heterogeneity in the permeability fields that are representative of randomly-connected, layered and fractured reservoirs. Finally, we discuss the applications of our results to real field cases of enhanced oil recovery by fluid injection.

1. INTRODUCTION

In recent times, there is a growing interest in integrating rock deformation with fluid flow processes in existing reservoir models to obtain a more realistic representation of the subsurface, improve production history matching and enhance model's prediction capability. Several studies of modeling hydrocarbon production, groundwater extraction, underground waste disposal, and CO₂ storage and sequestration have included the effect of geomechanical coupling in numerical models to successfully explain and predict the observed response of stress-sensitive formations. For example, a coupled numerical model combining chemical interactions between fluid and rock, mechanical deformation, and fluid advection and diffusion processes was tested to examine the mechanical stability of faulted caprock in a CO₂ sequestration project (Veer et al., 2015). In a study on shale gas (Wang et al., 2017), the authors found that in addition to key recovery mechanisms of gas adsorption, surface diffusion, and non-Darcy flow, stress-dependent permeability and porosity strongly affect the ultimate gas recovery factor. In another application, Jha and Juanes, 2014, proposed a computational approach to model coupled multiphase flow and geomechanics and simulate induced seismicity from fluid injection and withdrawal in faulted reservoirs. Moreover, rock deformation was

integrated into an analytical coupled hydro-mechanical solution of fluid injection into a finite cylindrical aquifer to improve the match between simulated and observed pressures (Simone and Carrera, 2017).

The spreading and mixing of particles in subsurface reservoirs have garnered significant interest, especially in real-time surveillance applications such as tracer analysis and waste disposal monitoring. It is also relevant for enhanced oil recovery methods such as chemical flooding and miscible gas injection (Jha et al., 2011a; Jha et al., 2011b; Jha et al., 2013). While spreading describes the spatial stretching and deformation of a solute slug driven by advective mechanisms, mixing is the mechanism that increases the actual fluid volume occupied by the solute behind the spreading front (Le Borgne et al., 2010). Spreading usually intensifies the solute concentration contrast in the domain while mixing tends to smooth out the concentration gradient within the solute-contaminated region. During enhanced oil recovery by gas injection, mixing is a key process driving the chemical injectant fluid and dictates the reaction rate at which reactants meet and interact (Bolster et al., 2010). Le Borgne et al., 2010, investigated the effect of permeability heterogeneity on temporal scaling properties of mixing and spreading to reveal alternate periods of non-Fickian mixing or spreading in heterogeneous velocity fields.

$$\mathbf{v} = \frac{k}{\mu}(\rho_f \mathbf{g} - \nabla p) \quad (4)$$

Above, k is the matrix permeability [meter²] assumed to be isotropic, μ is the fluid viscosity [Pascal*second], ρ_f is the fluid density [kg/meter³], and \mathbf{g} is the gravitational acceleration vector [meter/sec²].

- The linear momentum balance equations for fluid-saturated rock are

$$\nabla \cdot \boldsymbol{\sigma} + \rho_b \mathbf{g} = 0 \quad (5)$$

Above $\boldsymbol{\sigma}$ is the Cauchy total stress tensor [Pascal], ρ_b is the bulk density [kg/meter³]. A sign convention where the normal stresses are positive in tension is used.

- The transport equation with diffusion and advection processes is

$$D_d \nabla^2 c - \nabla \cdot (\mathbf{v}c) = \phi \frac{\partial c}{\partial t} \quad (6)$$

Here, D_d is the diffusion-dispersion coefficient [meter²/second], c is the normalized local concentration of tracer slug [dimensionless], and ϕ is the porosity. We make the transport equation dimensionless by defining the characteristic advection time as $t_{c,adv} = \phi h / v_c$, where the domain size h is the characteristic discretization length and v_c [meter/second] is the characteristic velocity. This defines the dimensionless Peclet number of the flow as $Pe = v_c h / D_d$.

- The effective stress equation is

$$\boldsymbol{\delta\sigma} = \boldsymbol{\delta\sigma}' - \alpha \delta p \mathbf{I}_d \quad (7)$$

where \mathbf{I}_d is the Identity Matrix. This equation relates the changes in total stress $\boldsymbol{\delta\sigma}$ and the fluid pressure variation δp to the change in effective stress $\boldsymbol{\delta\sigma}' = \mathbf{D}\boldsymbol{\varepsilon}$, where $\boldsymbol{\varepsilon}$ is the infinitesimal strain tensor. The Biot coefficient α is calculated from the solid grain bulk modulus K_s [Pascal] and the drained rock bulk modulus K ,

$$\alpha = 1 - \frac{K}{K_s} \quad (8)$$

and its value usually varies between the porosity value (for rocks with a high degree of cementation) to a maximum value of 1 (for soft soil).

- Biot's poroelasticity equation relating the fluid mass increment δm to the volumetric strain ε_v (normalized change in the pore volume, $\sigma_v = 3K\varepsilon_v$) and the pressure variation is

$$\frac{\delta m}{\rho_f} = \alpha \varepsilon_v + \frac{\delta p}{M} \quad (9)$$

2.3. Discretization

In this section, we discuss the scheme to numerically discretize the governing and constitutive equations mentioned above. To derive the weak forms of governing

equations for discretization, a standardized workflow is implemented consisting of the following steps: multiplication by an appropriate test function, integration over the domain, application of the divergence theorem, and imposition of Neumann and Dirichlet boundary conditions. The number of cells has been increased gradually from $N_x \times N_y = 20 \times 20$ to 100×100 to ensure convergence while the simulation runtime increases as expected and is within a manageable range of few hours. Here, N_x and N_y are the number of cells in the domain in X and Y directions.

Because of the different natures of flow, transport and mechanics problems, they are discretized differently. The flow problem is discretized in space using the 2nd order accurate finite volume method with cell-centered pressures and two-point flux approximation (TPFA). The mechanics problem is discretized using the standard finite element method with bilinear elements and nodal displacement vectors (Jha and Juanes, 2014). The transport problem is discretized using the 6th order accurate compact finite difference method (Lele, 1992).

The flow problem is integrated in time using the 1st order accurate implicit backward Euler scheme and the transport equation is integrated in time using the 3rd order accurate explicit Runge-Kutta scheme. Higher order schemes are used for the transport equation to resolve any sharp concentration fronts that might emerge in advection-dominated flows. The initial time step is calculated to be the minimum of the pressure diffusion time scale and the advection time scale. The characteristic time t_c [second] is defined as follows

$$t_c = \frac{\min(L_x, L_y)}{v_c} \quad (10)$$

$$= \frac{\min(L_x, L_y) \times \min(h_x, h_y)}{D_d Pe}$$

Above, L_x and L_y are the dimensions of the domain [meter], h_x and h_y are the cell dimensions [meter]. The maximum runtime of each simulation is set at $50t_c$. An adaptive time stepping method based on the Courant–Friedrichs–Lewy (CFL) condition is used to ensure stability. The dimensionless time step, Δt_d , is defined as

$$\Delta t_d = \frac{\max\left(\sqrt{v_x^2 + v_y^2}\right)}{\max(N_x, N_y)} \quad (11)$$

where v_x and v_y are the dimensionless velocities in X and Y directions, respectively. The CFL condition can be relaxed or tightened to ensure stability and smoothness of the coupled solution in each simulation sensitivity case.

2.4. Coupling strategy and solution scheme

In this section, we discuss the coupling strategy and the solution scheme for the coupled problem. The simulator utilizes a fully-coupled simultaneous solution approach to

solve for pressure and displacement fields at each time step. This is an unconditionally stable approach (Jha and Juanes, 2007; Kim et al., 2011; Jha and Juanes, 2014). One-way coupling between the flow-geomechanics solver and the transport solver is enforced by using the pressure field to calculate the velocity field as per Eq. (4). The following global matrices and vectors are assembled in the simulator from the cell matrices, which are evaluated using the four-point Gauss integration method within the finite element framework.

- Global transmissibility or mobility matrix A [meter²/Pascal/second]

$$A = \int_{\Omega} \frac{dN\mathbf{p}^T}{d\Omega} \frac{k}{\mu} \frac{dN\mathbf{p}}{d\Omega} d\Omega \quad (12)$$

where Ω is the 2D simulation domain area [meter²], and $N\mathbf{p}$ is the pressure shape function set to be the piecewise constant unit function over each cell.

- Global storativity or compressibility matrix S [meter²/Pascal]

$$S = \int_{\Omega} N\mathbf{p} \frac{1}{M} N\mathbf{p}^T d\Omega \quad (13)$$

- Global coupling matrix Q [meter]

$$Q = \int_{\Omega} N\mathbf{p} \alpha I_d L N d\Omega \quad (14)$$

where I_d is the identity vector [1 1 0] in 2D, L is the

differential operator $\begin{bmatrix} \frac{\partial}{\partial x} & 0 \\ 0 & \frac{\partial}{\partial y} \\ \frac{\partial}{\partial y} & \frac{\partial}{\partial x} \end{bmatrix}$ in 2D, N is the

displacement shape function defined using Lagrange polynomials.

- Global stiffness matrix K [Pascal]:

$$K = \int_{\Omega} \mathbf{B}^T \mathbf{D} \mathbf{B} d\Omega \quad (15)$$

where \mathbf{B} [per meter] is the strain-displacement matrix.

- Right-hand side of the mechanics equation (Neumann boundary and body force terms) f^u [Pascal*meter]:

$$f^u = \int_{\Gamma_u} N_t (\boldsymbol{\sigma} \mathbf{n}) d\Gamma + \int_{\Omega} N_t (\rho_b \mathbf{g}) d\Omega \quad (16)$$

where Γ_u denotes the Neumann boundary of the 2D domain, \mathbf{n} is the outward unit normal vector on that boundary, and N_t is the displacement shape function on the Neumann boundary.

- Right-hand side of the flow equation (boundary flux, gravitational flux) f^p (meter²/sec)

$$f^p = -\mathbf{q}^f N\mathbf{p}|_{\Gamma_p} + \int_{\Omega} \frac{dN\mathbf{p}}{d\Omega} \frac{k}{\mu} (\rho_f \mathbf{g}) d\Omega \quad (17)$$

where Γ_p denotes the flux boundary of the domain and \mathbf{q}^f is the outward flux on that boundary. The system of linear equations to solve becomes:

$$\begin{bmatrix} \mathbf{K} & -\mathbf{Q} \\ \mathbf{Q}^T & \mathbf{A} + \frac{\mathbf{S}}{\Delta t} \end{bmatrix} \begin{bmatrix} [u]^{n+1} \\ [p] \end{bmatrix} = \begin{bmatrix} f^u \\ f^p + \mathbf{Q}^T \frac{u^n}{\Delta t} + \mathbf{S} \frac{p^n}{\Delta t} \end{bmatrix} \quad (18)$$

The advection-diffusion transport equation is integrated in time using the 3rd order Runge-Kutta scheme. The dimensionless residual, Residual_{RK}, can be expressed as follows

$$\text{Residual}_{\text{RK}} = - \left[v_x \frac{dc}{dx} + v_y \frac{dc}{dy} + c \nabla \cdot \mathbf{v} - \frac{1}{Pe} \left(\frac{d^2 c}{dx^2} + \frac{d^2 c}{dy^2} \right) \right] \quad (19)$$

where the concentration derivatives are computed for the entire domain at once by multiplying the compact finite difference matrix (computed outside of the time loop) with the matrix of cell concentrations at the respective Runge-Kutta stages. $\nabla \cdot \mathbf{v}$ is the velocity divergence term calculated by applying the centered 2nd order accurate finite difference operator to the discrete velocity field. Note that for incompressible flows, $\nabla \cdot \mathbf{v} = 0$.

3. BASE CASE DESCRIPTION

3.1. Model parameters:

A Base Case is established with the values chosen to be realistic for the Physical Model described above (Table 1 and Table 2). The reservoir is assumed to be a relatively unconsolidated rock with a Young's modulus of 5 GPa. The coupling strength parameter, which indicates the degree of coupling between flow and mechanical processes is (Kim et al. 2011) as:

$$\tau = \frac{\alpha^2 M}{K} \quad (20)$$

Table 1: Base Case domain setup. Units used in the simulator are SI units.

Parameter	Symbol	Value
Number of cells in X direction	N_x	100
Number of cells in Y direction	N_y	100
Domain length in X direction	L_x	10 meters
Domain length in Y direction	L_y	10 meters
Boundary stress	prscSVal	10 Mpa
Boundary displacement	prscUVal	0 meter
Bottomhole flowing pressure	prscPVal	0.5 Mpa
Bottomhole injection rate	prscQVal	$18 \cdot 10^{-7}$ m ³ /sec

Table 2: Base Case parameters in SI units.

Parameter	Symbol	Value
Young Modulus	E	5 GPa
Poisson Ratio	ν	0.25
Grain Density	ρ_s	2650 kg/m ³
Bulk Modulus	K	3.33 GPa
Biot Modulus	M	4.73 GPa
Coupling Strength	τ	1.28
Diffusivity Coefficient	D_d	1 cm ² /sec
Peclet Number	Pe	10
Fluid Viscosity	μ	1.2*10 ⁻³ Pa*sec
Fluid Density	ρ_f	1000 kg/m ³
Fluid Compressibility	c_f	1*10 ⁻⁹ pa ⁻¹
Permeability	k	0.01*10 ⁻¹² m ²
Porosity	ϕ	0.2
Biot Coefficient	α	0.95

The boundary conditions of the flow problem are selected as follows. The pressure at the top boundary (location of the producer) is set equal to a typical bottomhole wellbore flowing pressure while injection rate at the bottom boundary (injector location) is set equal to 18*10⁻⁷ m³/sec (1 bbl/day). The injection rate is chosen based on the available pore volume of the domain (10 meters x 10 meters x porosity) such that it is approximately 1% of the volume. No-flow conditions are imposed on the left and right boundaries to model impermeable shale barriers outside the flow interval.

The boundary conditions of the transport problem are selected as follows. The bottom boundary is set to zero concentration of the tracer and the other three boundaries are open to the natural flow (zero concentration gradient in the normal direction) condition. These boundary conditions allow us to focus on the effect of flow-mechanics coupling on tracer mixing and spreading processes (Jha et al. 2013). Different types of boundary conditions and their counterparts in the real world are

Table 3: Problem Description with values for the mechanics, flow and transport sub-problems.

	Mechanics	Flow	Transport
Unknowns	Nodal displacement $\mathbf{U} = [U_x, U_y]$	Pressure p	Concentration c
Discretization method	Finite element	Finite volume	Finite difference
Dirichlet boundary conditions	Fixed boundary $U_x = 0$ or $U_y = 0$	Fixed pressure $p = \text{constant}$ or $p = 0$	Fixed concentration $C = 0$
Real scenarios analogous to the Dirichlet condition	Basement rock Wellbore wall	Bottom-hole pressure-controlled well or large aquifer	Sealed boundary
Neumann boundary conditions	Fixed traction σ $\sigma = 0$ or $\sigma = \text{constant}$	Fixed Rate q $q_f = 0$ or $q_f = \text{constant}$	Fixed concentration gradient $dc/dt=0$
Real scenarios analogous to the Neumann condition	Intact overlying rock or Stress-free surface	Impermeable boundary or constant injection rate	Natural open-flow
Initial conditions	Zero initial displacement $\mathbf{U}_0 = \mathbf{0}$	Initial pore pressure p_0	Customized Initial concentration c_0

3.2. Boundary conditions

The mathematical model requires well-defined boundary and initial conditions. Parts of the boundaries with prescribed Neumann and Dirichlet boundary conditions in a given coordinate direction should not overlap and together they should cover the entire boundary of the domain (Figure 1).

The boundary conditions of the mechanics problem are selected as follows. Constant compression stresses, representing the principal horizontal stresses at a reservoir depth of 2000 feet, are prescribed at the left and top boundaries. The bottom and right boundaries have zero normal displacement conditions. Applying both Dirichlet (fixed displacement) and Neumann (fixed stress) boundary conditions in each coordinate direction of the mechanics problem generalizes our simulation approach.

summarized in

Table 3.

3.3. Initial conditions

Initialization of coupled flow-geomechanical models is a non-trivial task. Ideally, the initial state (initial displacements and pressure) should be in mechanical and hydrostatic equilibria such that the initial strains and fluxes inside the domain are zero. This is partially achieved by prescribing a total initial stress tensor for each cell that balances the prescribed boundary stresses in each direction and by prescribing a hydrostatic initial pressure distribution that honors the fluid density (including the effects of depth-dependent compressibility and fluid-contacts in multiphase flow simulations). However, in complex sensitivity cases (such as spatially

variable Biot coefficient), the task to obtain zero initial displacements becomes challenging. A solution to this problem can be achieved in the simulations with linear elastic deformation by subtracting the initial displacement field from the displacement fields at subsequent time steps. This practice ensures a zero-displacement reference at the initial time step. The initial state of tracer slug is modeled as an instantaneously-placed uniform-concentration slug located near the injection well at the bottom boundary of the domain (Figure 2).

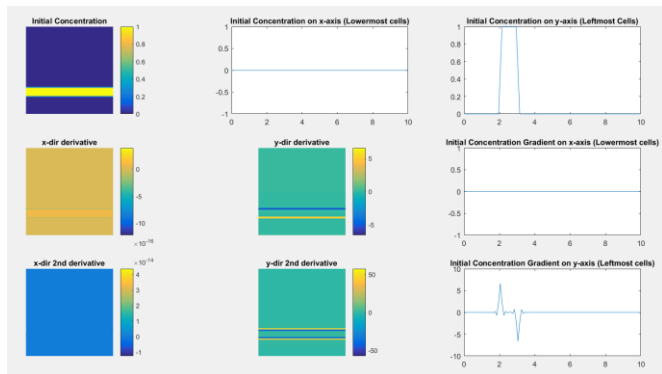


Figure 2: *Top left*: A uniform slug of tracer fluid (yellow strip). *Top right*: the concentration profile along the Y-axis with some smearing at the interfaces. *Middle and bottom rows*: The first and second order derivatives of the concentration field are calculated by the compact finite difference method. *Bottom right*: The two peaks of the concentration gradient along the Y-axis highlights the sharpness and uniformity of the slug.

3.4. Base Case output and results

Each simulation run provides nodal displacements (U_x and U_y), cell-centered pressure (p), edge-centered velocities (v_x and v_y) and cell-centered concentration (c). A simulation stops when the slug drains out of the domain completely, which is defined as the time when the maximum concentration at any cell does not exceed 0.01. The breakthrough time is defined as the time when the slug reaches the top boundary, i.e., the maximum concentration of all the cells near the top boundary exceeds 0.01. Depending on the magnitude of hydraulic diffusivity, which in turn depends on permeability, porosity, fluid viscosity and fluid compressibility, the steady state is attained at different times in different simulations. We are interested in observing the effects of geomechanical coupling and transient flow on the concentration variation of the slug before steady state is reached and pressure and displacement become constant with time. Therefore, a closer look at the simulation before the breakthrough time is necessary. Below we show the results of the Base Case simulation at two observation points shown as blue stars in Figure 1.

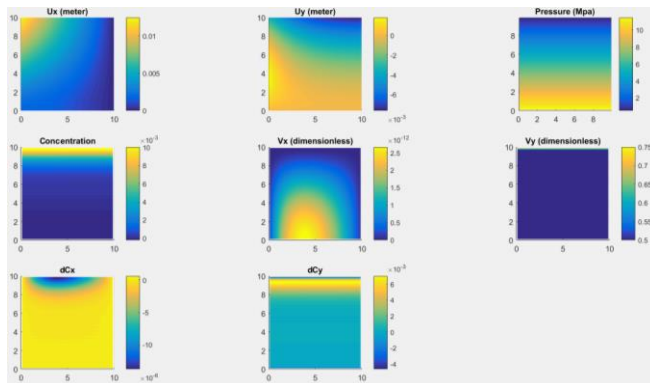


Figure 3: Base Case results (from left to right, top to bottom: U_x , U_y , p , c , v_x , v_y , dc/dx , dc/dy) at the end of the simulation.

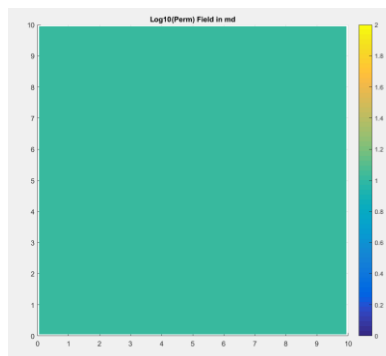


Figure 4: Base Case homogeneous permeability field ($\log k = 1$ or $k = 10$ md)

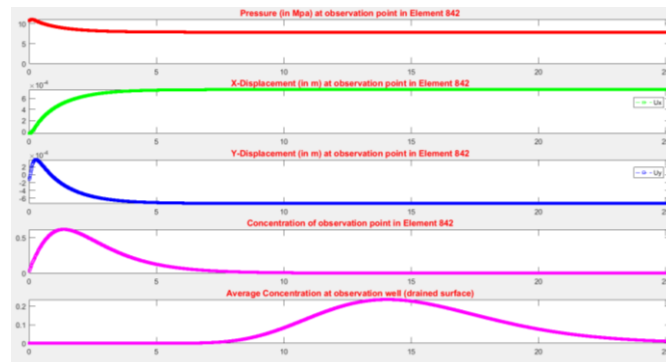


Figure 5: Base Case simulation results at the observation points. Time evolutions of pressure p_1 , displacements U_{x1} and U_{y1} , and concentrations c_1 and c_2 are shown from top to bottom. Subscripts 1 and 2 indicate 1st and 2nd observation points, respectively. The average concentration at the producer reaches its maximum value at $t_d = 13$ approximately, which signifies the arrival of the slug core.

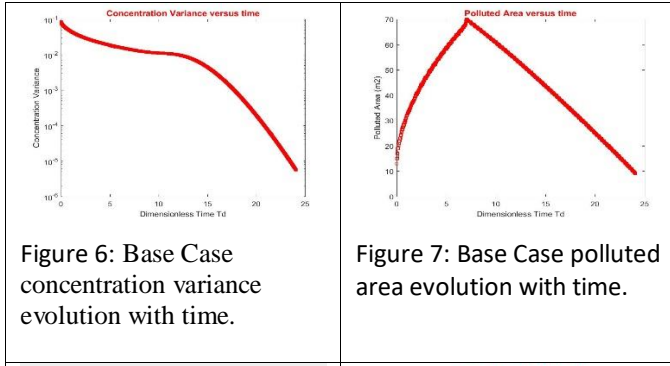


Figure 6: Base Case concentration variance evolution with time.

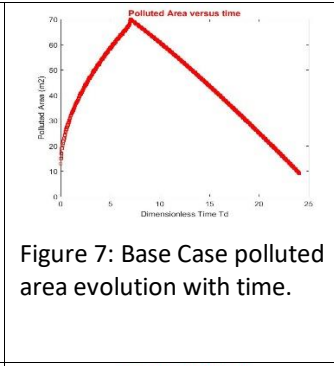


Figure 7: Base Case polluted area evolution with time.

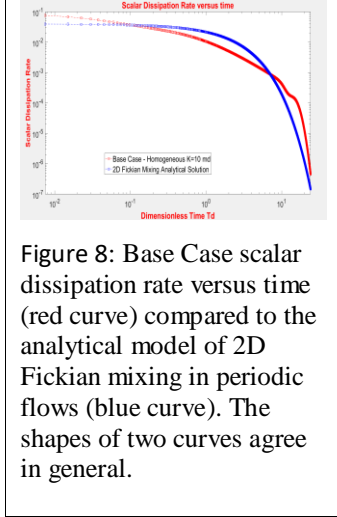


Figure 8: Base Case scalar dissipation rate versus time (red curve) compared to the analytical model of 2D Fickian mixing in periodic flows (blue curve). The shapes of two curves agree in general.

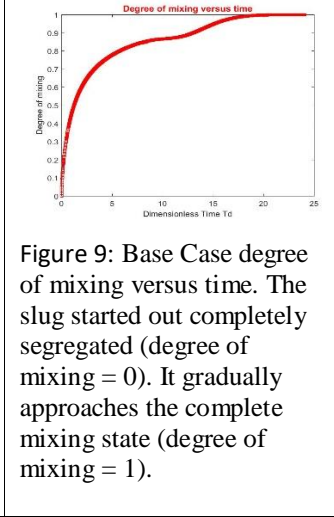


Figure 9: Base Case degree of mixing versus time. The slug started out completely segregated (degree of mixing = 0). It gradually approaches the complete mixing state (degree of mixing = 1).

As the pressure increases due to injection from the bottom injector, displacement in X and Y direction increases compared to the initial undeformed reference state. As the slug slowly moves upward and passes by the first observation point (Figure 1), it experiences increasing concentration at early times ($t_d \sim 0.1$) and decreasing concentration at later times. As the slug approaches the top boundary, the average concentration along the length of the producer observes increasing concentration at much later time ($t_d(\text{breakthrough}) = 7.4$). By the end of the simulation, the slug completely drains out from the top of the reservoir ($t_d(\text{drainage}) = 24.07$). These dimensionless times will be our parameters for evaluating the slug spreading processes in the domain. When spreading happens faster, we expect the breakthrough time to decrease. Spreading can also be characterized by the evolution of the area occupied by tracer (the polluted area) versus time (Figure 7). The polluted area is calculated as the area of cells in the mesh for which the cell concentration exceeds 0.005. The polluted area is expected to gradually increase with time before slug breakthrough and then decrease with time after slug breakthrough due to drainage from the top boundary.

The mixing process in porous media flows can be described by the mixing rate e.g. the scalar dissipation rate and the degree of mixing (Le Borgne et al., 2010; Jha et al., 2011a; 2011b; 2013). The degree of mixing, χ ,

quantifies the amount of mixing in the domain in terms of the concentration variance σ_c^2 . In dimensionless terms,

$$\sigma_c^2 = \langle c^2 \rangle - \langle c \rangle^2 \quad (19)$$

$$\chi(t) = 1 - \frac{\sigma^2(t)}{\sigma_{max}^2} \quad (20)$$

where $\langle \cdot \rangle$ denotes spatial averaging over the entire domain. In a perfectly mixed state, $\sigma_c^2 = 0$ and $\chi = 1$. In a completely segregated state, $\sigma_c^2 = \sigma_{max}^2$ and $\chi = 0$. The rate of mixing is quantified by the dimensionless scalar dissipation rate ϵ_c defined as:

$$\epsilon_c(t) = \frac{1}{Pe} \int_{\Omega} \nabla c(x, t) \cdot \nabla c(x, t) d\Omega \quad (21)$$

For Fickian or purely diffusive mixing of a linear slug transported through a homogeneous porous medium, the 1D analytical solution of the dissipation rate indicates a power-law slope of $-3/2$ in the $\log \epsilon_c - \log t$ plot (Le Borgne et al., 2010):

$$\epsilon_{c,1D}(t) = \frac{C_0^2 L_y t^{-3/2}}{8\sqrt{2\pi Pe}} \quad (22)$$

The evolution of the dimensionless scalar dissipation rate with dimensionless time in our simulation is shown in Figure 9, which shows an absence of a power-law behavior. Instead, the simulated behavior agrees better with the analytical model of dissipation rate in Fickian mixing of slugs in 2D periodic flows (Jha, 2014):

$$\epsilon_{c,2D}(t) = \frac{e^{-c_2 t}}{C_1 + \sqrt{tPe}} \quad (23)$$

Compared to the above analytical model, the simulated dissipation rate decays faster at early times, slower at intermediate times, and has a feature during the time window $t_d = 7-10$ which marks the breakthrough and draining of the slug. Therefore, the differences between the two curves are primarily due to the difference between the periodic flow boundary condition of the analytical model and non-periodic boundary condition of the simulation. These features contribute to the origin of non-Fickian mixing in the simulation.

4. SENSITIVITY ANALYSIS

4.1. Sensitivity model parameters

To better characterize the geomechanical effect, we perform a sensitivity analysis to investigate the influence of several key input parameters on the Base Case results. Parameters that are chosen in sensitivity analysis are Biot coefficient, fluid compressibility, stress boundary condition, permeability heterogeneity and material heterogeneity. These parameters are hypothesized to influence the coupling between geomechanical and transport problems. The values of these parameters are

chosen to represent real field scenarios that will be described in detail below.

4.2. Permeability heterogeneity

We introduce heterogeneity in the permeability field to better simulate real reservoirs. The geometric mean of the permeability field is kept constant in different cases and set equal to the homogenous Base Case (10 md). The variance of $\log_{10}(\text{permeability})$ and the correlation lengths of permeability in X and Y directions (ξ_x, ξ_y) are varied (see Figure 10). Case 1 and Case 2 describe a random permeability field with different magnitude variance. Case 3 and Case 4 depict channel-like features with different ranges of permeability. Compared to Case 3, Case 4 has higher maximum permeability ($\log k_{\max} = 2.5$ or $k_{\max} \sim 300$ md) and lower minimum permeability ($\log k_{\min} = -0.2$ or $k_{\min} \sim 0.6$ md) (Figure 10). Case 14 and Case 18 reduce the coupling strength by reducing the Biot coefficient of Case 1 and Case 4, respectively. This will help investigate the effect of geomechanical coupling in complex permeability fields.

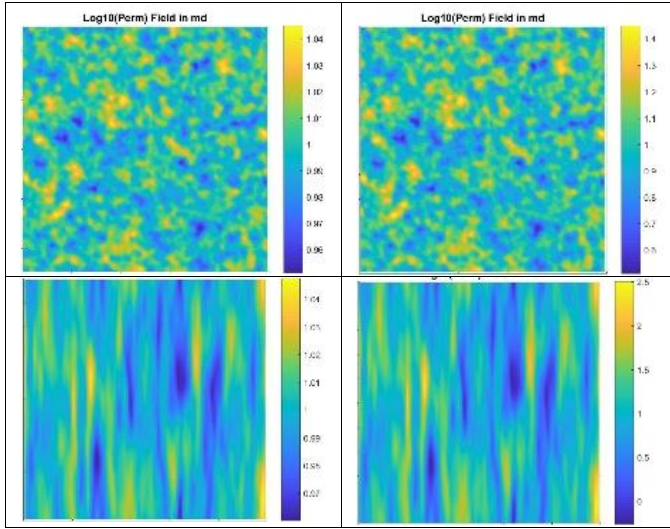


Figure 10: Heterogeneous permeability fields for sensitivity analysis. From left to right, top to bottom: Case 1 and Case 14 (Gaussian random permeability field with variance of $\log k = 0.001$, isotropic correlation length of 0.1 m), Case 2 (random permeability field with variance of $\log k = 0.1$), Case 3 (random permeability field with correlation length of 1 m in y-direction), Case 4 and Case 18 (random permeability field with variance of $\log k = 0.01$ and correlation length of 1 m in y-direction). Case 14 and Case 18 have lower Biot coefficient values (0.01) than the other cases (0.95).

Table 4: Sensitivity in the permeability heterogeneity

	Variance of $\log_{10}(k)$ (k in md)	ξ_x (m)	ξ_y (m)	α
Base Case	0	10	10	0.95
Case 1	0.001	0.1	0.1	0.95
Case 2	0.1	0.1	0.1	0.95
Case 3	0.001	0.1	1	0.95
Case 4	0.1	0.1	1	0.95

Case 14	0.001	0.1	0.1	0.01
Case 18	0.1	0.1	1	0.01

4.3. Coupling strength from degree of cementation and fluid compressibility

The coupling strength between flow and mechanics can be quantified by Eq. (20), where:

$$\tau = \frac{\alpha^2 M}{K}, \quad M = \frac{1}{\frac{\alpha - \phi}{K_s} + \phi c_f} \quad (24)$$

The Biot coefficient denotes the degree of cementation between the grains of the reservoir rock. It ranges from 1 (unconsolidated soil) to 0 (consolidated rock). For slightly compressible fluid, the fluid compressibility values range from $1.5 \cdot 10^{-10}$ to $2 \cdot 10^{-9}$ Pa^{-1} . Four cases are presented in Table 5.

Table 5: Sensitivity in the flow-mechanics coupling strength

Parameter	Biot Coefficient α	Fluid Compressibility c_f (Pa^{-1})	Coupling Strength τ
Base Case	0.95	10^{-9}	1.2817
Case 5	0.1	10^{-9}	0.0173
Case 6	0.5	10^{-9}	0.3061
Case 7	0.95	$2 \cdot 10^{-9}$	0.6584
Case 8	0.95	$0.5 \cdot 10^{-9}$	2.4337
Case 15	0	10^{-9}	0
Case 16	0.01	10^{-9}	0.0002

4.4. Regional stress condition

The boundary stress condition is varied to better capture the subsurface conditions where the minimum and maximum principal horizontal stresses are different and spatially changing because of the regional tectonic history. Thus, both magnitude (Figure 12) and spatial uniformity (Figure 13) of the horizontal stresses are included in the sensitivity analysis. Another case to consider is changing of in-situ stresses due to stress shadowing from hydraulic fracturing or the presence of natural fractures. This is modeled by imposing a non-uniform stress condition on the top boundary near the producer well (Figure 13).

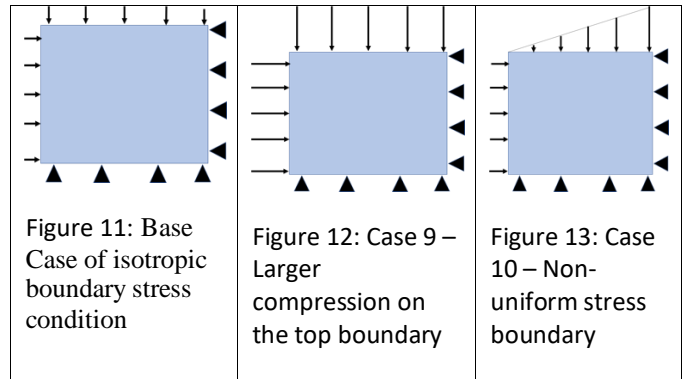


Figure 11: Base Case of isotropic boundary stress condition

Figure 12: Case 9 - Larger compression on the top boundary

Figure 13: Case 10 - Non-uniform stress boundary

Table 6: Sensitivity in the boundary stress condition

	Sh_{min} (MPa)	Sh_{max} (MPa)
Base Case	10	10
Case 9	15	15
Case 10	Linearly distributed	10
Case 19	5	5

4.5. Material heterogeneity

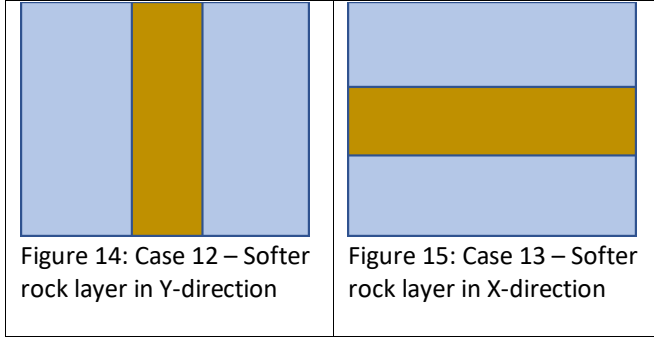


Figure 14: Case 12 – Softer rock layer in Y-direction

Figure 15: Case 13 – Softer rock layer in X-direction

Table 7: Softer rock elastic properties

Parameter	Symbol	Value
Young Modulus	E	1 MPa
Poisson Ratio	ν	0.33
Grain Density	ρ_s	2.4 g/cc
Bulk Modulus	K	0.98 GPa
Biot Modulus	M	4.93 GPa
Biot Coefficient	α	0.8
Permeability	k	10 md
Porosity	φ	0.05

We investigate the effect of a softer layer of rock embedded inside the domain. We consider two cases of the soft layer in X and Y directions, respectively (brown shades in Figure 14 and Figure 15). To isolate the effect of material heterogeneity on transport processes, the soft layer has the same permeability as the original matrix it replaces. Elastic properties of the soft layer are shown in Table 7.

5. DISCUSSION AND RESULT

5.1. Coupling strength from degree of cementation and fluid compressibility

When in-situ fluid becomes more compressible (c_f increases from $5 \cdot 10^{-10}$ to $2 \cdot 10^{-9}$ pa^{-1}) or the rock constituents become more cemented (α decreases from 0.95 to 0), the coupling strength between mechanics and flow processes decreases. The smallest value of coupling is expected when the in-situ fluid is highly compressible (gas-like) residing in a well-cemented rock. Spreading is

characterized by the dimensionless times of breakthrough and drainage. As the fluid becomes more compressible (from Case 8 to Base Case to Case 7), both drainage and breakthrough times decrease (Figure 16). This is because a higher value of fluid compressibility results in a lower Biot modulus value and a higher value of term $\left(\frac{1}{M} + \frac{\alpha^2}{K}\right)$ in Eq. (2), causing the velocity gradient term $\nabla \cdot v$ to decrease, which leads to a higher pressure gradient ∇p in Eq. (4). A higher pressure gradient in early pre-steady-state period results in higher velocities thereby decreasing the drainage and breakthrough times. On the other hand, as the rock becomes less cemented, both drainage and breakthrough times decrease (Figure 17). Extreme cases of very well-cemented rock are also tested when the Biot coefficient decreases to 0.01 and 0 to observe the effect of very weak and no coupling, respectively. These two cases yield similar drainage and breakthrough times, and both are higher than the cases of larger Biot coefficient values (Figure 17). Because α appears on both sides of Eq. (2), it is non-trivial to explain the dependence of pressure gradient and flow velocity on variation in α .

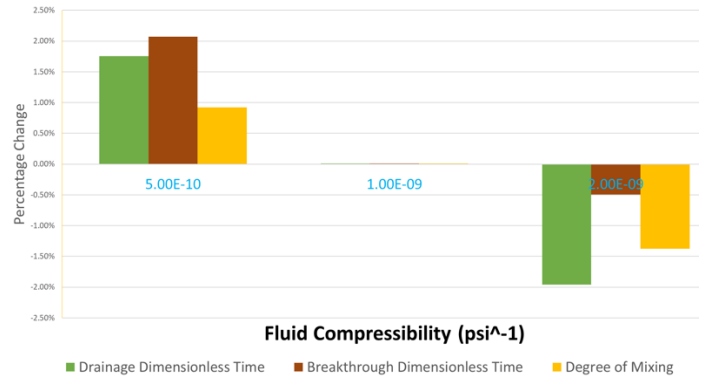


Figure 16: Effect of the fluid compressibility on the drainage time, breakthrough time and degree of mixing. The Base Case compressibility is $c_f = 10^{-9}$ psi^{-1} . Percentage change (y-axis) in the three quantities compared to their Base Case values are shown for two values of c_f , 5×10^{-10} and 2×10^{-9} psi^{-1} .

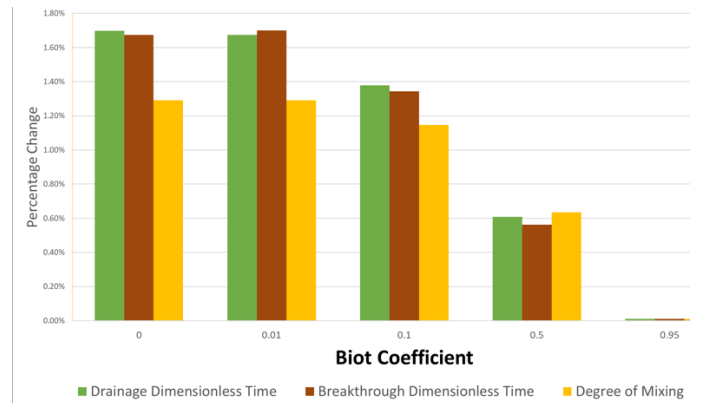


Figure 17: Effect of the Biot Coefficient on the drainage time, breakthrough time and degree of mixing. The Base Case Biot Coefficient is $\alpha = 0.95$. Percentage change in the three quantities compared to their base case values are shown for four different values of α .

Mixing is characterized by the evolution of the degree of mixing and scalar dissipation rate with time. At the breakthrough time of each simulation case, the degree of mixing is also recorded as χ_{BT} . There is a general trend of the degree of mixing decreasing with the Biot coefficient (Figure 17) and the fluid compressibility (Figure 16). This identifies two mechanisms of mixing weakening. Moreover, the above results suggest that the weakening mechanism of fluid compressibility is more significant than the weakening mechanism of Biot Coefficient.

5.2. Permeability heterogeneity

When we integrate permeability heterogeneity in the Base Case model, the general tendency is the increase of breakthrough and drainage times. In Case 1, a random permeability field is introduced with a non-zero variance of log permeability and shorter correlation lengths of permeability. As expected, low permeability values lead to longer drainage times (Table 8). In an extreme case (Case 4) of high log k variance and anisotropic correlation lengths, the slug is not able to drain from the domain after the maximum dimensionless time of $50t_c$ (Figure 18).

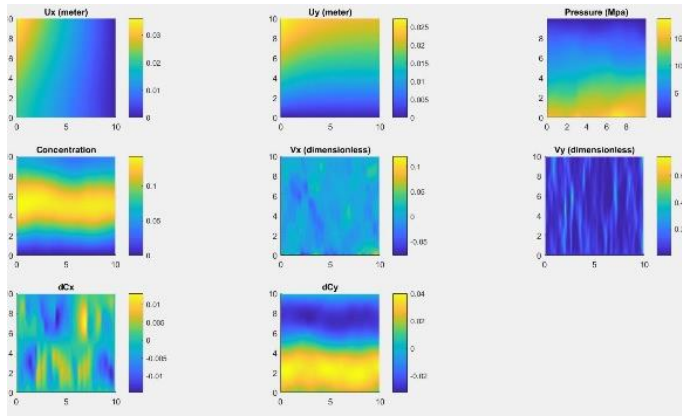


Figure 18: Case 4 simulation results. The variance of log k is increased to 0.1, and the correlation length in Y direction is increased to 1 m. Streaks of anomalously low and high velocity are present in the domain, and the concentration field shows advective twisting in the core and diffusive smearing at the interfaces.

In a milder heterogeneity case, Case 2 with log k variance of 0.1, low permeability values (less than 1 md) cause the drainage time to significantly increase from 25.7 in Case 1 to 44.8 in Case 2. The high streaks of permeability are not connected end-to-end in Y direction because of the short correlation length. Therefore, the breakthrough time of Case 2 is significantly greater than that of Case 1. In Case 3 (tenfold increase in the Y correlation length), the extreme low and high permeability cells are more aligned along the primary flow direction of the tracer slug. This situation slows down the slug movement in some areas and accelerates it in other areas, resulting in a slightly higher drainage time of 27.1 in Case 3 compared to 25.7 of Case 1 and a similar breakthrough time (7.8 compared to 7.7). In Case 14 compared to case 1, lower Biot coefficient leads to retardation of spreading in

heterogeneous permeability, further confirming the previous result of Section 5.1 in homogeneous permeability case.

Table 8: Breakthrough time, drainage time, degree of mixing at breakthrough for different permeability cases. The drainage time is not available for Case 4 and Case 18 because the slug did not finish draining during the simulation.

Parameter	t_d (breakthrough)	t_d (drain)	χ_{BT}
Base Case	7.375	24.070	0.837
Case 1	7.659	25.658	0.842
Case 2	10.211	44.818	0.884
Case 3	7.822	27.048	0.846
Case 4	22.156	N/A	0.953
Case 14	7.726	26.029	0.851
Case 18	11.680	N/A	0.906

The mixing of the slug is immensely affected by heterogeneity as expected (Nicolaidis et al., 2015). When log k variance is higher (Case 4 and Case 18), the degree of mixing increases significantly, especially in Case 4 where it reaches 0.95 at breakthrough. A longer breakthrough time in Case 4 allows the slug to linger and mix within the domain for a longer period, leading to a higher degree of mixing. This process of mixing augmentation is also manifested in the evolution of the mixing degree and dissipation rate (Figure 19 and Figure 20). At any pre-breakthrough time step, the degree of mixing is higher and the dissipation rate is lower for cases of higher heterogeneity (permeability variance). In Case 14 and Case 18 of which Biot coefficient values are low ($\alpha=0.01$) compared to Case 1 and Case 4 ($\alpha=0.95$), the degree of mixing is affected. However, the effect of permeability heterogeneity overwhelms the effect of Biot coefficient on mixing process in this study such that no clear trend is observed.

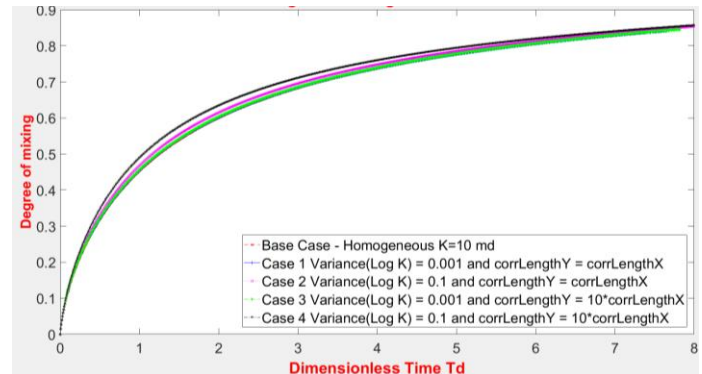


Figure 19: Evolution of the degree of mixing for different permeability cases.

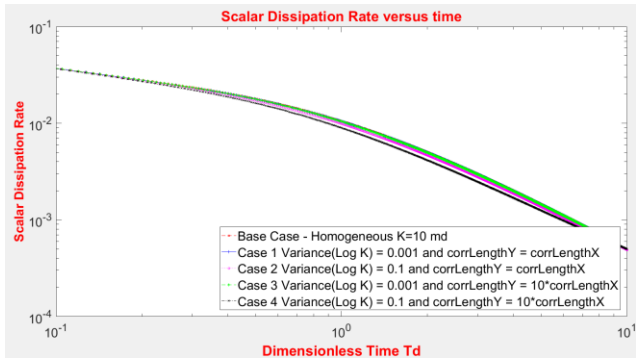


Figure 20: Evolution of the scalar dissipation rate for different permeability cases.

5.3. Regional stress condition

Boundary stress conditions are varied in terms of their magnitude and spatial distribution. Based on Figure 21, the larger the compressive stress imposed on boundaries, the higher the breakthrough and drainage times are. This means that a larger boundary compression prevents the slug from draining out of the domain and slows down the spreading process.

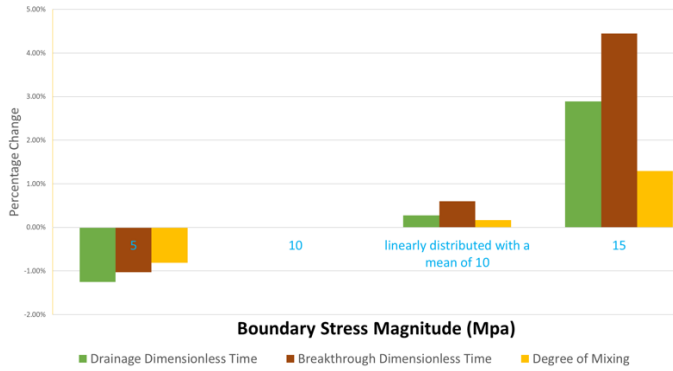


Figure 21: Effect of the boundary condition on spreading and mixing. This graph shows the percentage change of drainage time, breakthrough time and degree of mixing compared to their Base Case values. In the Base Case, the boundary stress is uniform with an isotropic compression at 10 MPa.

This causes a longer residence time for the slug and a higher degree of mixing as the boundary compression increases. The effect of the non-uniform distribution of the boundary load is captured in Case 10, where the load increases linearly along X direction (representing a linearly increasing shadow stress along the producer from multistage hydraulic fracturing). The effect of the non-uniform load distribution on the spreading and mixing behavior is insignificant for the studied cases.

5.4. Material heterogeneity

We insert an elastically soft layer of rock (called formation B) inside the original matrix (called formation A). U_x and U_y shown in Figure 22 and Figure 23 demonstrate the effect of formation B's orientation. In Case 12 where formation B is aligned along Y direction, breakthrough and drainage times increase and the

opposite happens when formation B is aligned along X direction in Case 13 (Table 9). In Case 13, because of the softer material in the transverse direction (X direction), the increase of geomechanical coupling in the longitudinal direction (Y direction, the direction of macroscopic slug movement) enhances spreading and leads to shorter breakthrough and drainage times.

Table 9: Breakthrough time, drainage time, degree of mixing at breakthrough for different material heterogeneity cases

	Base Case	Case 12	Case 13
t_d (breakthrough)	7.375	7.823	7.247
t_d (drainage)	24.07	24.953	23.627
χ_{BT}	0.837	0.849	0.826

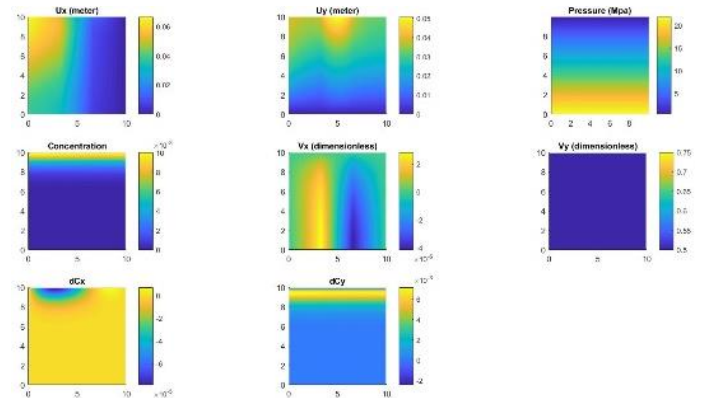


Figure 22: Case 12 (softer layer aligned along Y-direction) simulation results at the end of the simulation.

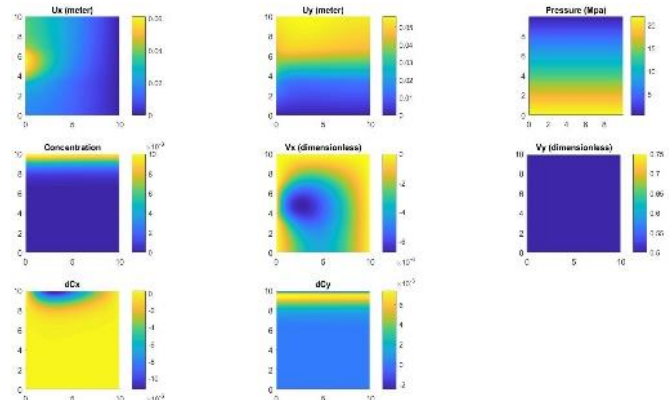


Figure 23: Case 13 (softer layer aligned along X-direction) simulation results at the end of the simulation.

Figure 24 and Figure 25 show that Case 13 is very similar to Base Case. This implies that the presence of a softer formation perpendicular to the direction of slug movement does not affect mixing significantly. On the contrary, the inclusion of a softer rock layer parallel to the macroscopic direction of slug movement enhances the mixing process by a small amount.

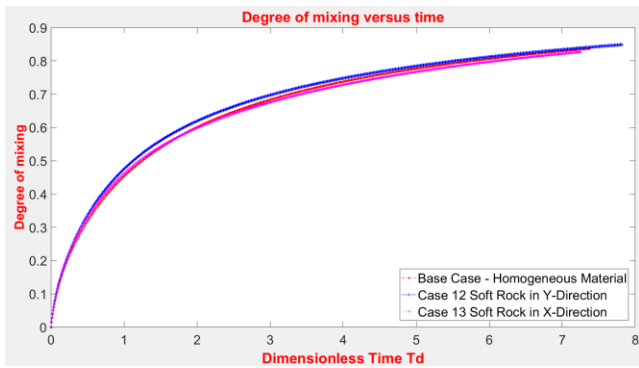


Figure 24: Evolution of the degree of mixing for different material heterogeneity cases.

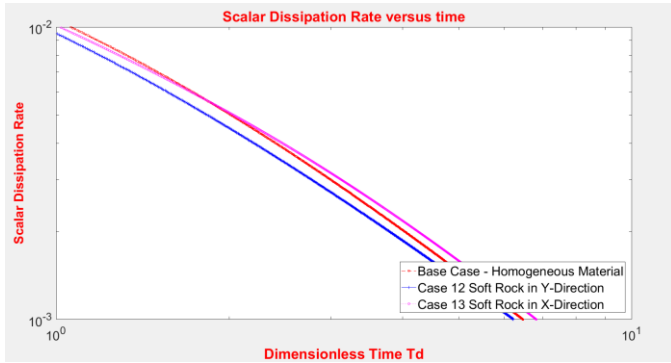


Figure 25: Evolution of the rate of mixing for different material heterogeneity cases.

6. SUMMARY AND CONCLUSION

We investigated the effect of rock deformation on the spreading and mixing of a passive tracer in a 2D deformable poroelastic media using numerical simulations. Motivated by the difference in the mathematical nature of the governing equations, we proposed a numerical formulation of fully-coupled flow-geomechanics with one-way coupled transport via the velocity field. A sensitivity analysis was performed to obtain the extent of geomechanical influence on the macroscopic transport quantities, namely the breakthrough time, the drainage time, the degree of mixing and the dissipation rate during mixing. The sensitivity analysis considered the heterogeneity in permeability field, the fluid compressibility, the Biot coefficient, tectonic load magnitude and distribution, and the material heterogeneity. The parameters and their values were chosen to represent real-world scenarios.

The results show that the strength of coupling between flow and geomechanics processes influence the transport of the slug as manifested by variations in the macroscopic transport parameters. Factors that can retard the spreading process are high permeability variance, the presence of soft rock parallel to the direction of slug movement, and high boundary compression. On the other hand, higher fluid compressibility, higher Biot coefficient, and the presence of soft rock perpendicular to the slug movement direction tend to enhance spreading. The primary factor

that retards the mixing process is a higher fluid compressibility (e.g. aquifers and oil reservoirs compared to gas reservoirs) or a higher Biot coefficient (deeper and sandstone reservoirs compared to shallower and limestone reservoirs). High permeability variance, high compression on the boundary, and the presence of soft rock parallel to the slug movement direction enhances mixing. The presence of soft material in the direction transverse to slug movement does not affect mixing.

There will be situations where it takes much longer time to reach steady state (constant velocity field), for example, in flows with more viscous fluid, lower matrix permeability or higher porosity rock. In those cases, we should expect a more pronounced signature of geomechanical effect on spreading and mixing because the velocity field will be affected by rock deformation over longer durations.

The model has a tremendous amount of flexibility and can be extended to capture complicated situations, such as stress-dependent flow properties (porosity and permeability), effect of gravity and buoyancy, effect of source/sink, and presence of fractures. One-way coupling between transport and geomechanics could be extended to incorporate dependency of transport properties on non-linear geomechanical processes e.g. shear dilation, partial fabric collapse, and joint aperture dilation (Dusseault, 2008). In addition, the coupling between transport and geomechanics could be upgraded to two-way coupling by introducing the feedback from concentration-dependent hydromechanical properties (fluid viscosity, density, and compressibility) and the effect of mixing into the mechanical deformation process.

7. NOMENCLATURE

A	Biot Coefficient (dimensionless)
M	Biot modulus (Pascal)
ρ_b	Bulk density (kg/meter ³)
K	Bulk modulus (drained) (Pascal)
h_x, h_y	Cell dimension in X and Y direction (meter)
v_c	Characteristic advective velocity (meter/second)
t_c	Characteristic time (second)
C	Concentration (dimensionless)
ξ_x, ξ_y	Correlation length in X, Y direction (meter)
Q	Coupling matrix (meter)
T	Coupling strength
L	Differential operator tensor
$t_{d(Breakthrough)}$	Dimensionless breakthrough time

t_d (drainage)	Dimensionless drainage time
D_d	Diffusion coefficient (meter ² /sec)
Δt_d	Dimensionless timestep
U_x	Displacement in X direction (meter)
U_y	Displacement in Y direction (meter)
\mathbf{N}_t	Displacement shape function
\mathbf{U}	Displacement vector (meter)
L_x, L_y	Domain size in X and Y direction (meter)
\mathbf{D}	Elasticity tensor (Pascal)
d	Eulerian dimension of space (dimensionless)
q	Flow rate (meter ³ /sec)
ρ_f	Fluid density (kg/meter ³)
μ	Fluid viscosity (Pascal*sec)
K_s	Grain bulk modulus (Pascal)
\mathbf{g}	Gravitational acceleration (meter/second ²)
\mathbf{I}_d	Identity vector [1 1 0]
C_o	Initial concentration (dimensionless)
p_o	Initial pressure (Pascal)
Γ_p	Neumann boundary of flow
Γ_u	Neumann boundary of mechanics
N_x, N_y	Number of cells in X, Y direction
Pe	Peclet number
k	Permeability (meter ²)
ν	Poisson Ratio (dimensionless)
ϕ	Porosity
P	Pressure (Pascal)
\mathbf{N}_p	Pressure shape function
Ω	Simulation Domain
\mathbf{K}	Stiffness matrix (Pascal)
\mathbf{S}	Storativity matrix (meter ² /Pascal)
\mathbf{B}	Strain displacement matrix
σ	Stress tensor (Pascal)
t	time (second)
\mathbf{A}	Transmissibility matrix (m ² /Pa/sec)
\mathbf{V}	Velocity vector (meter/second)
σ_v	Volumetric Stress (Pascal)
E	Young modulus (Pascal)

8. REFERENCE

- Bolster, D., D.A. Benson, T. Le Borgne, and M. Dentz. 2010. Anomalous mixing and reaction induced by superdiffusive nonlocal transport. *Physical Review E - Statistical, Nonlinear, and Soft Matter Physics*, 82(2), 1–5.
- Coussy, O., 2004. *Poromechanics*. John Wiley & Sons.
- De Simone, S. and J. Carrera. 2017. Analytical solutions to coupled hydro-mechanical problems to highlight the nonlocal nature of aquifer storage. *Water Resources Research*, 53(11), 9580–9599.
- Dusseault, M.B., 2008, September. Coupling geomechanics and transport in petroleum engineering. In *Proc. SHIRMS Int. Conf on Geomechanics*.
- Jha, B., Cueto-Felgueroso, L., & Juanes, R., 2011a. Fluid mixing from viscous fingering. *Physical Review Lett*, 106. doi:10.1103/PhysRevLett.106.194502
- Jha, B., L. Cueto-Felgueroso. and R. Juanes. 2011b. Quantifying mixing in viscously unstable porous media flows. *Physical Review E*, 84(6), doi: 10.1103/PhysRevE.84.066312
- Jha, B., Cueto-Felgueroso, L., & Juanes, R., 2013. Synergetic Fluid Mixing from Viscous Fingering and Alternating Injection. *Physical Review Lett*, 106, doi: 10.1103/PhysRevLett.111.144501
- Jha, B., & Juanes, R., 2014. Coupled multiphase flow and poromechanics: A computational model of pore pressure effects on fault slip and earthquake triggering. *Water Resources Research*, 50, doi:10.1002/2013WR015175.
- Jha, B., 2014. *Flow Through Porous Media: From Mixing of Fluids to Triggering of Earthquakes*, Ph.D. Thesis, MIT
- Jing, L., K.B. Min, A. Baghbanan, and Z. Zhao. 2013. Understanding coupled stress, flow, and transport processes in fractured rocks. *Geosystem Engineering*, 16(1), pp.2-25.
- Kim, J., H.A. Tchelepi, and R. Juanes. 2009. Stability, accuracy and efficiency of sequential methods for coupled flow and geomechanics. In *SPE reservoir simulation symposium*. Society of Petroleum Engineers.
- Le Borgne, T., M. Dentz, D. Bolster, J. Carrera, J.R. De Dreuzy, and P. Davy. 2010. Non-Fickian mixing: Temporal evolution of the scalar dissipation rate in heterogeneous porous media. *Advances in Water Resources*, 33(12), pp.1468-1475.
- Lele, S.K., 1992. Compact finite difference schemes with spectral-like resolution. *Journal of computational physics*, 103(1), pp.16-42.
- Nicolaides, C., B. Jha, L. Cueto-Felgueroso, and R. Juanes. 2015. Impact of viscous fingering and permeability heterogeneity on fluid mixing in porous media. *Water Resources Research*, 51(4), pp.2634-2647.
- Rutqvist, J., C. Leung, A. Hoch, Y. Wang, and Z. Wang. 2013. Linked multicontinuum and crack tensor approach for modeling of coupled geomechanics, fluid flow, and transport in fractured rock. *Journal of Rock Mechanics and Geotechnical Engineering*, 5(1), pp.18-31.

Veer, E.F., S. Van Der Waldmann, and P.A. Fokker. 2015. November. A Coupled Geochemical-Transport-Geomechanical Model to Address Caprock Integrity During Long-Term CO₂ Storage. In 49th US Rock Mechanics/Geomechanics Symposium. American Rock Mechanics Association.

Wang, J., H. Luo, H. Liu, F. Cao, Z. Li, and K. Sepehrnoori. 2017. An integrative model to simulate gas transport and production coupled with gas adsorption, non-Darcy flow, surface diffusion, and stress dependence in organic-shale reservoirs. *SPE Journal*, 22(01), pp.244-264.